

Supplementary Information Appendix

Antonelli, Pester, Brown, DePaolo; PNAS, 2017.

Sections:

I. SI Text

1. Reaction-Path Modeling
2. Charge-Balance Model
3. Comments on Hydrothermal Reaction rates
 - a. Ca,Sr Exchange Factor
 - b. Dual Porosity Model

II. SI References

III. SI Figures

- S1 – Hydrothermal Ca from GWB and natural vents
- S2 – Schematic Flowchart for charge balance calculations
- S3 – Sr addition and removal during precipitation of anhydrite-2
- S4 – Sr concentrations in modern hydrothermal vent fluids
- S5 – Dual porosity model results

I. SI Text

1. Reaction-Path Modeling

Equilibrium reaction path models were constructed to test the relative effects of precursor seawater chemistry on the Ca concentration of mid-ocean ridge hydrothermal fluids in the context of the charge-balance simplification presented in the main text (equation [1]). Geochemist's Workbench was used for the simulations (1) along with a 500 bar thermodynamic database that includes mineral solid-solution chemistry (2). Thermodynamic data for Mg-hydroxy-sulfate-hydrate (MHS) was also included (3), and combined effects of anhydrite and MHS precipitation were calibrated using additional experimental data (4, 5). However, MHS proved to be unstable in the presence of silicates during preliminary models and was ultimately suppressed for simplicity in the final calculations.

Two main groups of simulations were conducted at four different temperatures ranging from 250 to 400°C (Fig. S1). The first simulations use modern seawater and the others use average Cretaceous seawater, represented by NaCl balanced solutions with [Mg]:[Ca]:[SO₄] of 53:10:28 and 30:30:10, respectively (mmol/kg).

In all scenarios, one kg of starting solution is heated to the initial temperature of interest (250-400°C), which causes the precipitation of anhydrite until either Ca or SO₄ is fully removed. The isothermal solution is then reacted with basalt by incrementally adding small amounts to the system. The bulk mineral assemblage of the basalt consists of: plagioclase (An₇₅) : olivine (Fo₈₀) : diopside : enstatite : hedenbergite : pyrrhotite, in the mass ratio 0.69 : 0.21 : 0.063 : 0.018 : 0.019 : 0.003 (pyrrhotite was added as an appropriate source of reduced sulfur).

The results of the simulations, along with data from modern hydrothermal vents, are plotted in Fig. S1. When seawater [Ca] < [SO₄], as in modern systems, a second phase of anhydrite formation occurs as seawater Mg is exchanged for basaltic Ca. The cumulative amount of anhydrite precipitated is shown as dashed red lines. The simulations show that all of the sulfate is removed before dissolved Ca begins to increase in the fluids, in agreement with the two stages of anhydrite precipitation in our Sr-isotope model.

After sulfate is removed and Mg has been fully replaced with basaltic Ca, the compositions of the fluids increasingly diverge with decreasing water/rock ratio (W/R < ~10), with differences depending largely on the phase equilibria for different temperatures. In both scenarios, the models predict that below ~350 °C, albitic plagioclase becomes increasingly stable with decreasing *T*, resulting in a small fraction of seawater Na being removed to accommodate additional dissolved Ca in the fluids. Above 350 °C, calcic plagioclase and amphibole are increasingly stable, drawing down Ca and increasing dissolved Na and Fe in the fluids (not shown). Generally, albitization drives [Ca] upwards at lower temperatures, and amphibole precipitation drives [Ca] downwards at higher temperatures, as corroborated by modern hydrothermal vent fluids (Fig. S1c). The dominant secondary silicates that form in all simulations are chlorite, tremolite, and secondary plagioclase solid solutions, along with small amounts of epidote when *T* < 400 °C.

Despite the variability at different temperatures, we note that the average [Ca] values are approximately the same as for average modern vent fluids (~30-35 mM) (6, 7), which represent an integration of many different fluid flow-paths and temperatures. Model results between 300 and

400°C using modern seawater (Fig. S1a) agree with the concentration range of dissolved [Ca] in hydrothermal fluids sampled from the Mid-Atlantic Ridge, Juan de Fuca Ridge, and the East Pacific Rise (Fig. S1c), when normalized to seawater chlorinity to account for the effects of fluid phase separation (8). Generally, at higher water/rock ratios the reaction path for Ca is nearly independent of T because the removal of seawater Mg to hydrous alteration minerals is thermodynamically favorable at all conditions.

When using Cretaceous seawater we notice two important differences (Fig. S1b), the first is that it comes into the system with much higher Ca (~20 mM) than modern seawater, which has not been titrated by prior anhydrite precipitation, and that the Ca concentration for all simulated temperatures is higher than for modern vents. This model serves to indicate that seawater calcium was more likely to persist through hydrothermal circulation at times of high seawater Ca/SO₄ and low Mg/Ca, with conservative paleoseawater estimates suggesting average vent fluids contained up to ~40% seawater calcium (e.g. Fig. 2), instead of ~0% as is suggested by $\delta^{44}\text{Ca}$ signatures in modern hydrothermal vents (9–11). The simulation results in Fig. S1 should also encompass reactions with more ultramafic lithologies because models run with lower primary plagioclase fractions (not shown) exhibit less T -dependent variability beyond the Mg titration stage.

From the GWB simulations, we infer that the average composition of the fluids after full titration of seawater components is a good estimate of average modern high-temperature hydrothermal vent fluids when considering the natural range in compositions (Fig. S1c). In the modern ocean, the exit temperature of hydrothermal fluids is loosely correlated with the amount of dissolved [Ca]_{hyd}, likely due to phase equilibria at different temperatures. The average [Sr]_{hyd} we use in our model (~110 μM) is from a compilation of published values for hydrothermal vent fluids corrected for phase separation (Fig. S4).

2. Charge-Balance Model

Following the logic put forward in the main text (shown schematically in Fig. S2), the losses and gains of Sr are tied to the losses and gains of Ca. We define the variables in equations [4, 5] as follows:

$$[\text{Sr}]_{\text{Anh1}} = R_{\text{anh}} \begin{cases} [\text{SO}_4]_{\text{sw}} & \text{if } [\text{Ca}]_{\text{sw}} > [\text{SO}_4]_{\text{sw}} \\ [\text{Ca}]_{\text{sw}} & \text{if } [\text{Ca}]_{\text{sw}} < [\text{SO}_4]_{\text{sw}} \end{cases} \quad [\text{S1}]$$

The strontium lost during anhydrite-2 precipitation is a combination of seawater Sr ($[Sr]_{anh2,sw}$) and Sr gained from the basalts. The total amount of Ca released from basalt (counter-balanced by a loss of seawater Mg) and captured as anhydrite-2 is defined:

$$[Ca]_{Anh2} = \begin{cases} 0 & \text{if } [Ca]_{sw} > [SO_4]_{sw} \\ \{[SO_4]_{sw} - [Ca]_{sw}\} & \text{if } [Ca]_{sw} < [SO_4]_{sw} \end{cases} \quad [S2]$$

The amount of basaltic and seawater Sr in the fluids after each step of anhydrite-2 precipitation is calculated iteratively in 1-mmol increments of Ca (ΔCa) until sulfate is fully removed, from $n = 0$ to $n = [Ca]_{Anh2}$, such that:

$$[Sr]'_{bslt}(n+1) = [Sr]'_{bslt}(n) + \Delta Ca R_{bslt} - \Delta Ca R_{anh} \left[\frac{[Sr]'_{bslt}(n) + R_{bslt}}{[Sr]'_{sw}(n) + [Sr]'_{bslt}(n) + R_{bslt}} \right] \quad [S3]$$

$$[Sr]'_{sw}(n+1) = [Sr]'_{sw}(n) - \Delta Ca R_{anh} \left[\frac{[Sr]'_{sw}(n)}{[Sr]'_{sw}(n) + [Sr]'_{bslt}(n) + R_{bslt}} \right] \quad [S4]$$

Where $[Sr]'_{bslt}$ and $[Sr]'_{sw}$ are the amounts of basaltic and seawater Sr in the hydrothermal fluids after n steps of sulfate removal, respectively. $[Sr]'_{bslt}(n=0)$ equals zero, and $[Sr]'_{sw}(n=0)$ equals $[Sr]_{sw} - [Sr]_{anh1}$, which is the strontium left over after primary anhydrite precipitation.

Therefore, the amount of seawater Sr lost to anhydrite-2 is:

$$[Sr]_{anh2,sw} = [Sr]_{sw} - [Sr]_{anh1} - [Sr]'_{sw}(n = [Ca]_{Anh2}) \quad [S5]$$

And the overall amount of basaltic Sr gained by the fluids after anhydrite-2 formation is:

$$[Sr]_{bslt1} = [Sr]'_{bslt}(n = [Ca]_{Anh2}) \quad [S6]$$

The effects of anhydrite-2 formation on the seawater and basaltic $[Sr]$ in the fluids are depicted in Fig. S3. After complete removal of seawater sulfate as anhydrite, the remaining seawater Mg then exchanges with basaltic Ca, releasing a proportional amount of basaltic Sr such that:

$$[Sr]_{bslt2} = R_{bslt} \{[Mg]_{sw} - [Ca]_{anh2}\} \quad [S7]$$

Further exchange is required to arrive at the average Sr isotopic composition for modern vents. We define the high-temperature Ca,Sr exchange:

$$[Sr]_{exch} = [Ca]_{hyd} \theta_{exch} R_{bslt} \quad [S8]$$

Where θ_{exch} is the fraction of total hydrothermal Ca that exchanges with basalt after the Mg-Ca charge balance has been satisfied. The value of θ_{exch} is calibrated from modern hydrothermal systems ($\theta_{\text{exch}} = 0.108$) [*e.g.* ~11% of modern $[\text{Ca}]_{\text{hyd}}$ needs to exchange with basalt with stoichiometric Sr/Ca (R_{bslt}) to arrive at $^{87}\text{Sr}/^{86}\text{Sr} = 0.7037$].

Previous iterations of our final model, which included models using i) different Sr/Ca ratios for anhydrite-1 and anhydrite-2, ii) variations in the high-T Ca,Sr exchange factor (θ_{exch}), and iii) variable Sr/Ca according to various distribution coefficients (using GWB), yield the same results as our final model with only slight differences in the amplitude of the $^{87}\text{Sr}/^{86}\text{Sr}$ oscillations.

3. Comments on hydrothermal reaction rates

a. Ca,Sr Exchange Factor

Hydrothermal fluid compositions could be further changed if paleoseawater chemistry also induced differences in chemical reaction rates during hydrothermal circulation. The model presented in the main text does not incorporate any potential differences in seawater-basalt exchange rates due to paleoseawater chemistry. However, it is unlikely that there are no changes to the kinetics of the discussed chemical reactions due to differences in the composition of seawater, especially at lower temperatures.

Experimental studies of hydrothermal basalt alteration have shown that a large pH drop accompanies the precipitation of secondary Mg-OH minerals (13), and experimental and modeling work has shown that lower pH values can speed up basalt dissolution by several orders of magnitude (14), with small effects still predicted to persist at high temperatures (15). This implies that precipitation of Mg-OH minerals may serve to increase the exchange rates between seawater and basalt, and thus could have additional kinetic effects on the composition of hydrothermal fluids. A large pH drop especially accompanies the precipitation of MHS phases (3, 5, 16), which are likely to be the metastable precursors of anhydrite-2, and this effect may have been completely absent in Paleoseawater with $[\text{Ca}] > [\text{SO}_4]$ (Figs. 2, S1, S2).

If the removal of dissolved Mg from the hydrothermal fluid as it circulates through the system is responsible for acidifying the fluid (5, 13), then at times of low seawater $[\text{Mg}]$, hydrothermal fluids might be less acidified and hence less reactive. Any slowing of the reaction between basalt and hydrothermal fluid would enhance the likelihood of seawater Sr and Ca persisting through the

hydrothermal system and increase their presence in the fluid budget at the vents, which would increase the $^{87}\text{Sr}/^{86}\text{Sr}$ of exiting hydrothermal fluids.

A first-order attempt at exploring the potential dependence of seawater-basalt exchange rates on seawater Mg concentrations is made by scaling θ_{exch} with $[\text{Mg}]_{\text{sw}}$ according to:

$$\theta(t) = \theta(0) \left\{ \frac{[\text{Mg}]_{\text{sw}}(t)}{[\text{Mg}]_{\text{sw}}(0)} \right\}^m \quad [\text{S9}]$$

This formulation allows us to vary the fluid-basalt exchange to assess its effect on the results. Our base model in the main text is $m = 0$, and we evaluate the results for m up to 3. In all of the cases where $m \neq 0$, this factor serves to subtly increase the amount of recycled seawater Sr in hydrothermal output fluids by decreasing the seawater-basalt exchange, but would have much greater effects if θ_{exch} (calculated to be ~ 0.108 for modern) was larger.

b. Dual Porosity Model

To explore possible changes in reaction rates from another point of view, we construct a steady state dual-porosity model for hydrothermal fluids based on previous work (17). The parameters are set such that modern seawater exits the system with average vent fluid $^{87}\text{Sr}/^{86}\text{Sr}$ compositions. This allows us to then explore the effects of changing $[\text{Sr}]$ and reaction rates (Fig S5).

The dual-porosity model assumes steady state with no change in porosity (dissolution = precipitation rate), and represents flow through a fracture with chemical diffusion supplying basaltic components from the walls. The model applies well to hydrothermal Sr isotopic evolution in systems like MOR where circulation is dominated by fluid flow in fractures. The essential effect of fractures is that the extent of exchange depends on the amount of chemical communication between fractures and bulk matrix. The latter is determined by the ratio of diffusivity and the reaction rates in the inter-fracture rock matrix [parameter denoted as “R” by (17)].

The dual-porosity model constructed has parameters set so that emergent fluids have $^{87}\text{Sr}/^{86}\text{Sr} = 0.7037$ when using modern seawater (other input parameters given in the figure caption). We then explore the effects of increasing $[\text{Sr}]$ and reducing reaction rates in order to simulate potential differences resulting from changes in paleoseawater composition. The modern case (position “A” on Fig. S5) is calculated assuming the initial fluid $[\text{Sr}]$ is $\sim 35 \mu\text{M}$ due to Sr removal associated with earlier anhydrite precipitation, consistent with our previous charge-balance calculations. The

parameters used then require that the reaction rate, R , be about 0.0003 yr^{-1} to match modern $^{87}\text{Sr}/^{86}\text{Sr}$ output. The units mean that 0.03% of the rock mass dissolves (and reprecipitates as secondary minerals) each year.

To evaluate the difference with paleoseawater, the model is modified so that the initial fluid has $[\text{Sr}]$ of $285 \mu\text{M}$ in order to simulate higher seawater $[\text{Sr}]$ and lower losses to anhydrite, as suggested by our Cretaceous charge-balance models. With higher levels of seawater $[\text{Sr}]$ entering the reaction zone, the exiting fluid was calculated to increase to 55% seawater Sr, position “B” on figure S5, despite having the same reaction rate as the first simulation. When we additionally decreased the reaction rate by an arbitrary factor of three (0.0001 yr^{-1}), the $^{87}\text{Sr}/^{86}\text{Sr}$ increased to 71% SW Sr, position “C” on figure S5. Contours for constant seawater Sr fractions in the exiting hydrothermal fluids for various reaction rates and $[\text{Sr}]$ concentrations remaining after sulfate removal are also shown.

The dual porosity model indicates that an arbitrary three-fold decrease in reaction rate relative to modern would result in a ~15-20% increase in seawater-derived Sr in the exiting fluids, with greater differences as seawater $[\text{Sr}]$ increases (Fig. S5). From this model, we conclude that relatively small changes in reaction rates for hydrothermal exchange, associated with variable paleoseawater chemistry, would lead to fairly significant changes in the $^{87}\text{Sr}/^{86}\text{Sr}$ of hydrothermal fluids. However, reaction rate data for dissolution/precipitation of individual minerals and experimental work using modified seawater compositions will be necessary in order to construct a realistic model for MOR hydrothermal systems, which would ideally include reactive transport modeling and kinetic effects.

II. Supplemental References

1. Bethke CM (2008) *Geochemical and Biogeochemical Reaction Modeling* (Cambridge University Press, New York). 2nd Ed. doi:10.1017/CBO9781107415324.004.
2. Pester NJ, et al. (2012) Subseafloor phase equilibria in high-temperature hydrothermal fluids of the Lucky Strike Seamount (Mid-Atlantic Ridge, 37°17'N). *Geochim Cosmochim Acta* 90:303–322.
3. Janecky DR, Seyfried WE (1983) The solubility of magnesium-hydroxide-sulfate-hydrate in seawater at elevated temperatures and pressures. *Am J Sci* 283(8):831–860.
4. Bischoff JL, Rosenbauer RJ (1983) A note on the chemistry of seawater in the range 350 - 500 C. *Geochim Cosmochim Acta* 47(1):139–144.
5. Bischoff JL, Seyfried WEJ (1978) Hydrothermal chemistry of seawater from 25 degrees to 350 degrees C. *Am J Sci* 278(6):838–860.
6. Von Damm K. L, et al. (1985) Chemistry of submarine hydrothermal solutions at 21 °N, East Pacific Rise. *Geochim Cosmochim Acta* 49(11):2197–2220.
7. Elderfield H, Schultz a. (1996) Mid-Ocean Ridge Hydrothermal Fluxes and the Chemical Composition of the Ocean. *Annu Rev Earth Planet Sci* 24(1):191–224.
8. Pester NJ, Ding K, Seyfried WE (2015) Vapor–liquid partitioning of alkaline earth and transition metals in NaCl-dominated hydrothermal fluids: An experimental study from 360 to 465°C, near-critical to halite saturated conditions. *Geochim Cosmochim Acta* 168:111–132.
9. Amini M, et al. (2008) Calcium isotope ($d_{44}/40\text{Ca}$) fractionation along hydrothermal pathways, Logatchev field (Mid-Atlantic Ridge, 14 45 N). *Geochim Cosmochim Acta* 72(16):4107–4122.
10. Bach W, Humphris SE (1999) Relationship between the Sr and O isotope compositions of hydrothermal fluids and the spreading and magma-supply rates at oceanic spreading centers. *Geology* 27(12):1067–1070.
11. Pester NJ, Syverson DD, Higgins JA, Seyfried WEJ (2016) Ca and Sr isotope Systematics in mid-ocean ridge hydrothermal fluids. *Abstract V53E-02, Fall Meeting, AGU, San Francisco, CA*, p 1.
12. Flaathen TK, Gislason SR, Oelkers EH (2010) The effect of aqueous sulphate on basaltic glass dissolution rates. *Chem Geol* 277(3–4):345–354.
13. Seyfried WE, Bischoff JL (1981) Experimental seawater-basalt interaction at 300 C, 500 bars, chemical exchange, secondary mineral formation and implications for the transport

- of heavy metals. *Geochim Cosmochim Acta* 45(2):135–147.
14. Gudbrandsson S, Wolff-Boenisch D, Gislason SR, Oelkers EH (2011) An experimental study of crystalline basalt dissolution from 2pH1 and temperatures from 5 to 75 C. *Geochim Cosmochim Acta* 75(19):5496–5509.
 15. Aradóttir ESP, Sigfússon B, Sonnenthal EL, Björnsson G, Jónsson H (2013) Dynamics of basaltic glass dissolution - Capturing microscopic effects in continuum scale models. *Geochim Cosmochim Acta* 121:311–327.
 16. Haymon RM, Kastner M (1986) Caminite : A new magnesium-hydroxide-sulfate-hydrate mineral found in a submarine hydrothermal deposit, East Pacific Rise , 21°N. *Am Mineral* 71:819–825.
 17. DePaolo DJ (2006) Isotopic effects in fracture-dominated reactive fluid-rock systems. *Geochim Cosmochim Acta* 70(5):1077–1096.
 18. Butterfield DA, et al. (1997) Seafloor eruptions and evolution of hydrothermal fluid chemistry. *Philos Trans R Soc A Math Phys Eng Sci* 355(1723):369–386.
 19. Butterfield DA, Massoth GJ (1994) Geochemistry of north Cleft segment vent fluids: Temporal changes in chlorinity and their possible relation to recent volcanism. *J Geophys Res Solid Earth* 99(B3):4951–4968.
 20. Butterfield DA, Massoth GJ, McDuff RE, Lupton JE, Lilley MD (1990) Geochemistry of hydrothermal fluids from Axial Seamount hydrothermal emissions study vent field, Juan de Fuca Ridge: Subseafloor boiling and subsequent fluid-rock interaction. *J Geophys Res* 95(B8):12895.
 21. Campbell AC, et al. (1988) Chemistry of hot springs on the Mid-Atlantic Ridge. *Nature* 335(6190):514–519.
 22. Charlou J., et al. (2000) Compared geochemical signatures and the evolution of Menez Gwen (37°50'N) and Lucky Strike (37°17'N) hydrothermal fluids, south of the Azores Triple Junction on the Mid-Atlantic Ridge. *Chem Geol* 171(1–2):49–75.
 23. Charlou J., Donval J., Fouquet Y, Jean-Baptiste P, Holm N (2002) Geochemistry of high H₂ and CH₄ vent fluids issuing from ultramafic rocks at the Rainbow hydrothermal field (36°14'N, MAR). *Chem Geol* 191(4):345–359.
 24. Charlou JL, et al. (1996) Mineral and gas chemistry of hydrothermal fluids on an ultrafast spreading ridge: East Pacific Rise, 17° to 19°S (Naudur cruise, 1993) phase separation processes controlled by volcanic and tectonic activity. *J Geophys Res Solid Earth* 101(B7):15899–15919.

25. Edmond JM, et al. (1995) Time series studies of vent fluids from the TAG and MARK sites (1986, 1990) Mid-Atlantic Ridge: a new solution chemistry model and a mechanism for Cu/Zn zonation in massive sulphide orebodies. *Geol Soc London, Spec Publ* 87(1):77–86.
26. Foustoukos DI, Pester NJ, Ding K, Seyfried WE (2009) Dissolved carbon species in associated diffuse and focused flow hydrothermal vents at the Main Endeavour Field, Juan de Fuca Ridge: Phase equilibria and kinetic constraints. *Geochemistry, Geophys Geosystems* 10(10):n/a-n/a.
27. Foustoukos DI, Seyfried WE (2007) Quartz solubility in the two-phase and critical region of the NaCl–KCl–H₂O system: Implications for submarine hydrothermal vent systems at 9°50'N East Pacific Rise. *Geochim Cosmochim Acta* 71(1):186–201.
28. Gallant RM, Von Damm KL (2006) Geochemical controls on hydrothermal fluids from the Kairei and Edmond Vent Fields, 23°–25°S, Central Indian Ridge. *Geochemistry, Geophys Geosystems* 7(6):n/a-n/a.
29. Grimaud D, Michard A, Michard G (1984) Composition chimique et composition isotopique du strontium dans les eaux hydrothermales sous-marines de la dorsale Est Pacifique a 13° Nord. *C R Acad Sc Paris* 299:865–870.
30. Kumagai H, et al. (2008) Geological background of the Kairei and Edmond hydrothermal fields along the Central Indian Ridge: Implications of their vent fluids' distinct chemistry. *Geofluids* 8(4):239–251.
31. Michard G, et al. (1984) Chemistry of solutions from the 13°N East Pacific Rise hydrothermal site. *Earth Planet Sci Lett* 67(3):297–307.
32. Pester NJ, Rough M, Ding K, Seyfried WE (2011) A new Fe/Mn geothermometer for hydrothermal systems: Implications for high-salinity fluids at 13°N on the East Pacific Rise. *Geochim Cosmochim Acta* 75(24):7881–7892.
33. Seyfried WE, Pester NJ, Ding K, Rough M (2011) Vent fluid chemistry of the Rainbow hydrothermal system (36°N, MAR): Phase equilibria and in situ pH controls on subseafloor alteration processes. *Geochim Cosmochim Acta* 75(6):1574–1593.
34. Seyfried WE, Seewald JS, Berndt ME, Ding K, Foustoukos DI (2003) Chemistry of hydrothermal vent fluids from the Main Endeavour Field, northern Juan de Fuca Ridge: Geochemical controls in the aftermath of June 1999 seismic events. *J Geophys Res Solid Earth* 108(B9). doi:10.1029/2002JB001957.
35. Von Damm KL (2000) Chemistry of hydrothermal vent fluids from 9°–10°N, East Pacific Rise: “Time zero,” the immediate post-eruptive period. *J Geophys Res Solid Earth*

105(B5):11203–11222.

36. Von Damm KL (2004) Evolution of the hydrothermal system at East Pacific Rise 9°50'N: Geochemical evidence for changes in the upper oceanic crust. *Mid-Ocean Ridges: Hydrothermal Interactions Between the Lithosphere and Oceans*, eds German CR, Lindsay J, Parson LM (American Geophysical Union, Washington DC), pp 285–305. geophys. M.
37. Von Damm KL, Bray AM, Buttermore LG, Oosting SE (1998) The geochemical controls on vent fluids from the Lucky Strike vent field, Mid-Atlantic Ridge. *Earth Planet Sci Lett* 160(3–4):521–536.
38. Von Damm KL, Parker CM, Gallant RM, Loveless JP (2002) Chemical Evolution of Hydrothermal Fluids From EPR 21° N: 23 Years Later in a Phase Separating World. *American Geophysical Union, Fall Meeting* doi:2002AGUFM.V61B1365V.
39. Butterfield DA, et al. (1994) Gradients in the composition of hydrothermal fluids from the Endeavour segment vent field: Phase separation and brine loss. *J Geophys Res Solid Earth* 99(B5):9561–9583.
40. Pester NJ, Ding K, Seyfried WE (2014) Magmatic eruptions and iron volatility in deep-sea hydrothermal fluids. *Geology* 42(3):255–258.
41. Reeves EP, et al. (2011) Geochemistry of hydrothermal fluids from the PACMANUS, Northeast Pual and Vienna Woods hydrothermal fields, Manus Basin, Papua New Guinea. *Geochim Cosmochim Acta* 75(4):1088–1123.

III. SI Figures S1-S5

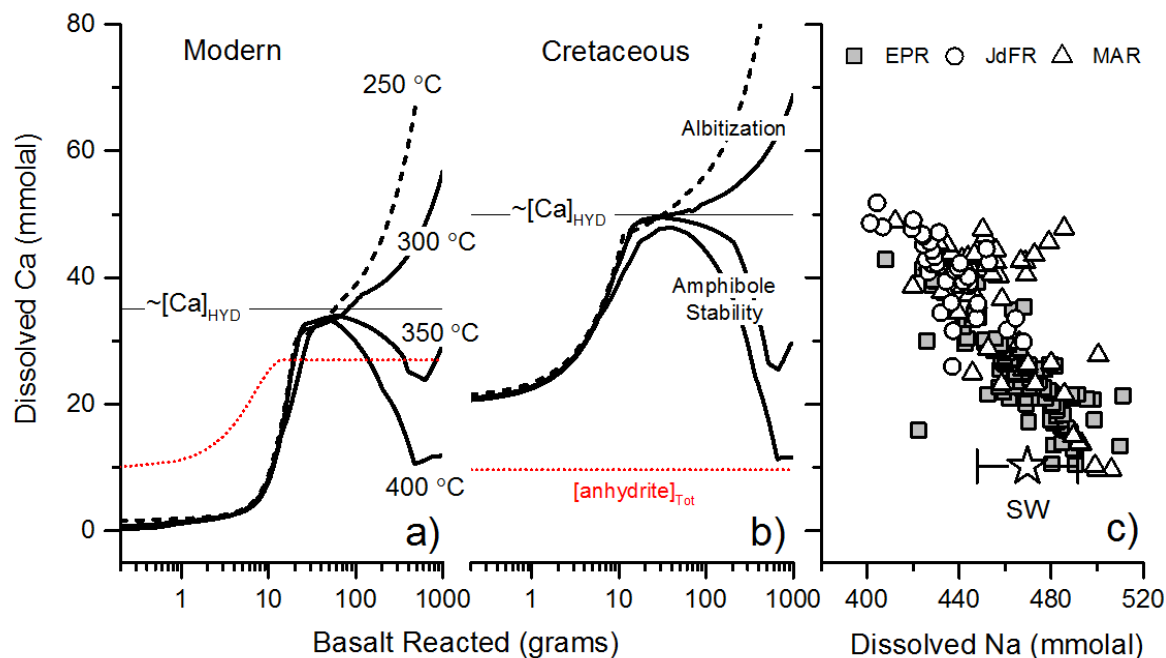


Fig. S1. Evolution of dissolved [Ca] in hydrothermal reaction-path models where 1 kg of basalt is incrementally added to 1 kg of (a) modern seawater and (b) estimated Cretaceous seawater. Individual curves represent independent isothermal simulations between 250 and 400 °C, cumulative milliequivalents of precipitated anhydrite are shown for reference (red dotted line, see text). 250 °C calculations (dashed) were truncated at fluid/rock = 2 (500 g basalt reacted). In (c) error on [Na] in seawater reference point (star) reflects general uncertainty in evaluating charge balance compensation with [Ca] in vent fluids due to the order of magnitude higher concentration. Vent fluid data are from various sources (2, 6, 18–38).

Hydrothermal mass-balance model summary chart

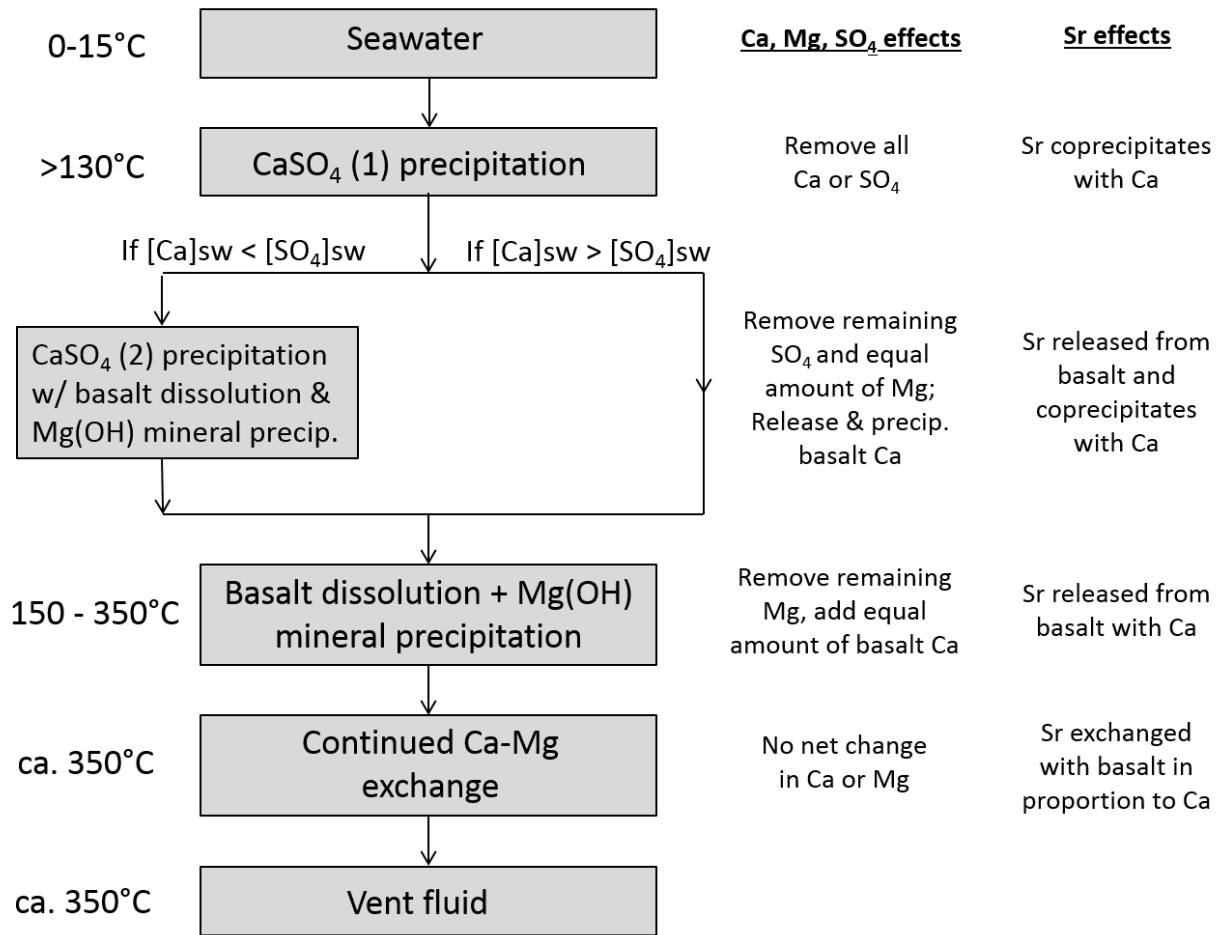


Fig. S2. Schematic for hydrothermal model, showing the four major steps discussed in the main text.

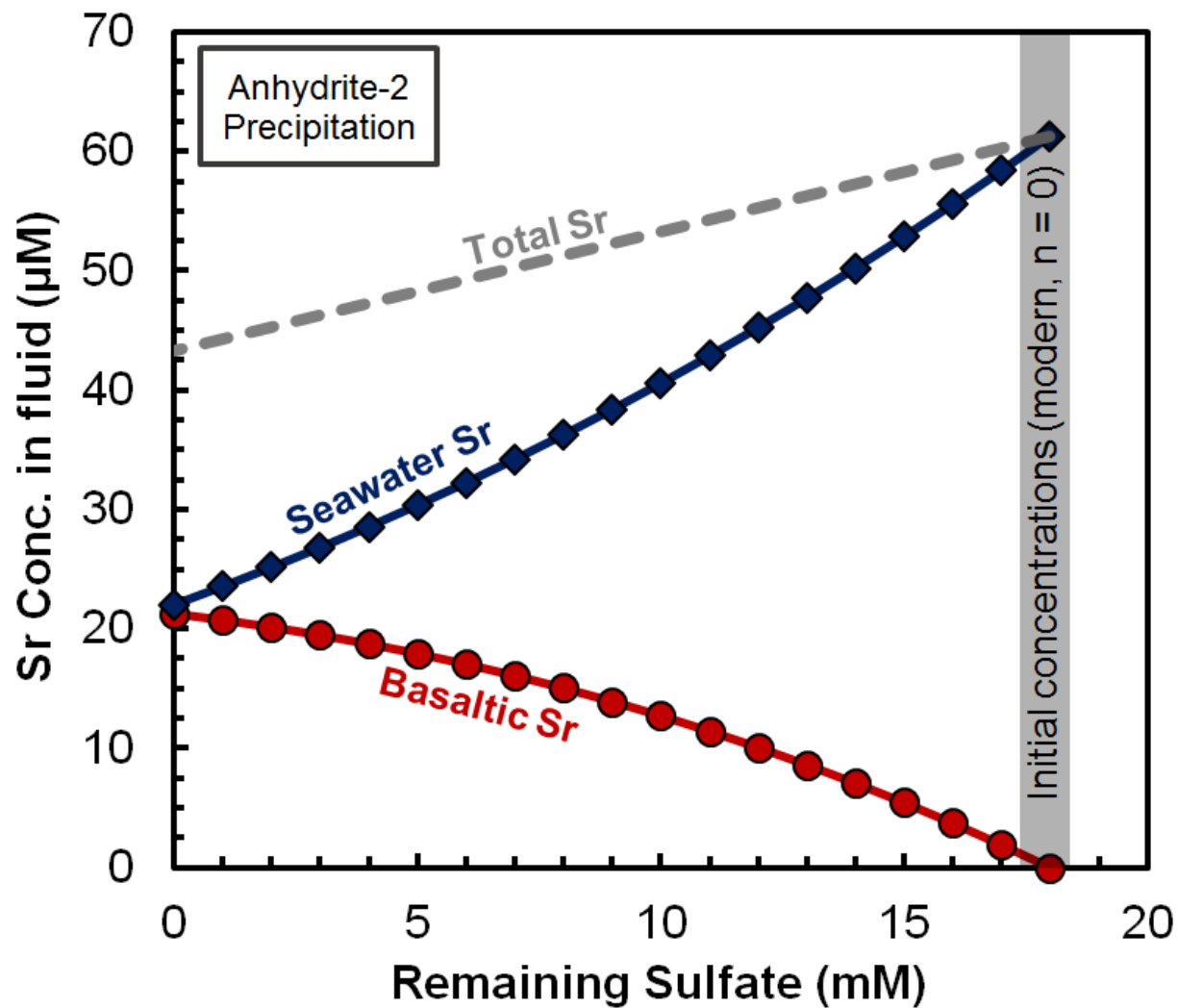


Fig. S3. Sr concentrations during precipitation of anhydrite-2 using modern seawater input values. Lines represent [Sr] in the evolving hydrothermal fluid: grey line is total [Sr], blue line is seawater [Sr], and red line is basaltic [Sr]. Initial Sr is equal to $[Sr]_{SW} - [Sr]_{anh1}$ (at $n=0$) and the number of steps (n) in the iterative calculation is equal to $[Ca]_{anh2}$, according to equations [S3] through [S6]; In the modern case, $[Ca]_{anh2} = 18$.

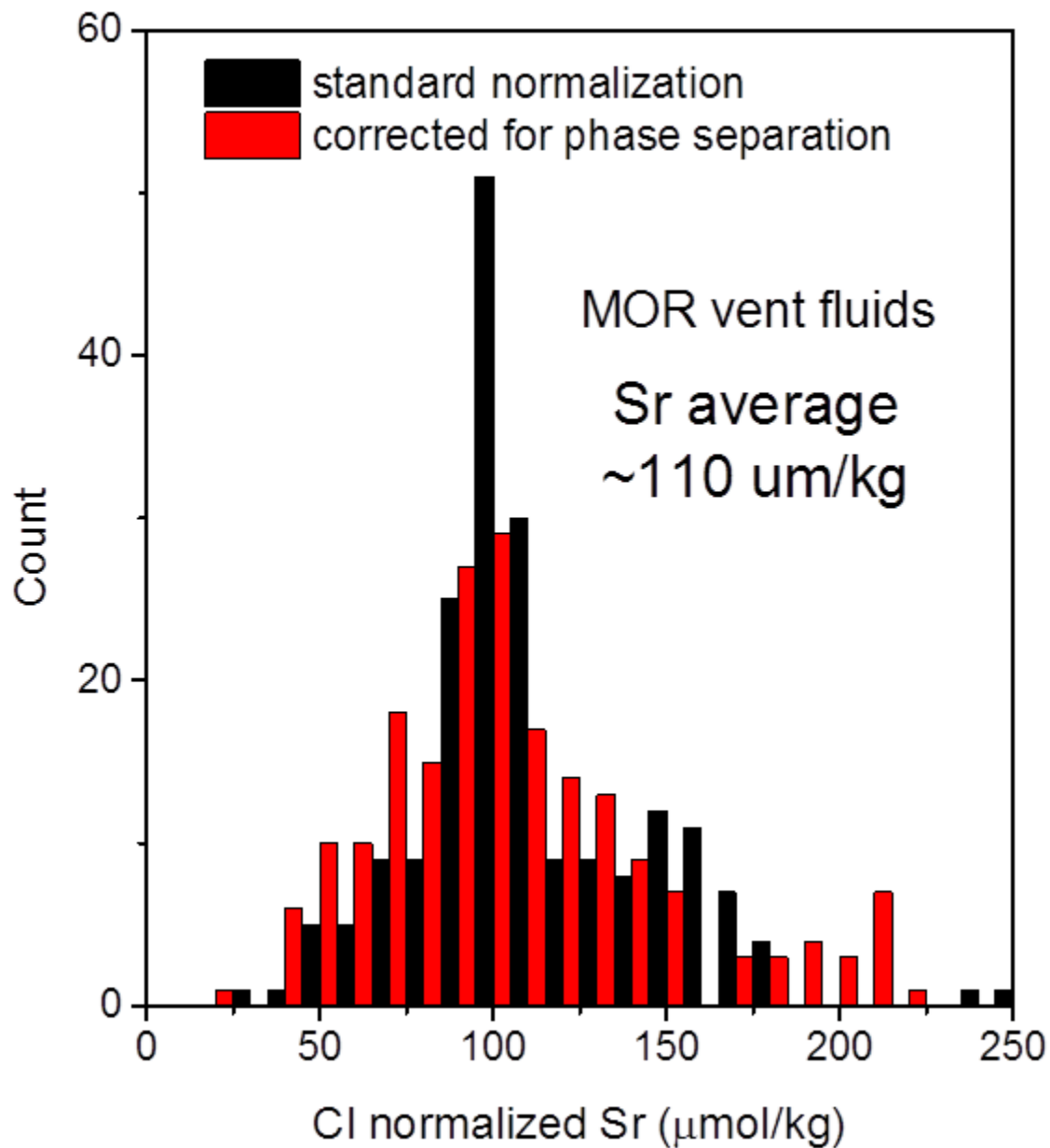


Fig. S4. Histogram of end-member [Sr] values in deep-sea hydrothermal fluids, normalized to seawater chlorinity ($[\text{Cl}]_{\text{sw}} = 548 \text{ mmol/kg}$). Standard normalization (black bars) and a normalization accounting for partitioning due to phase separation (8) (red bars) are both presented. Data are from various sources (2, 6, 18–41).

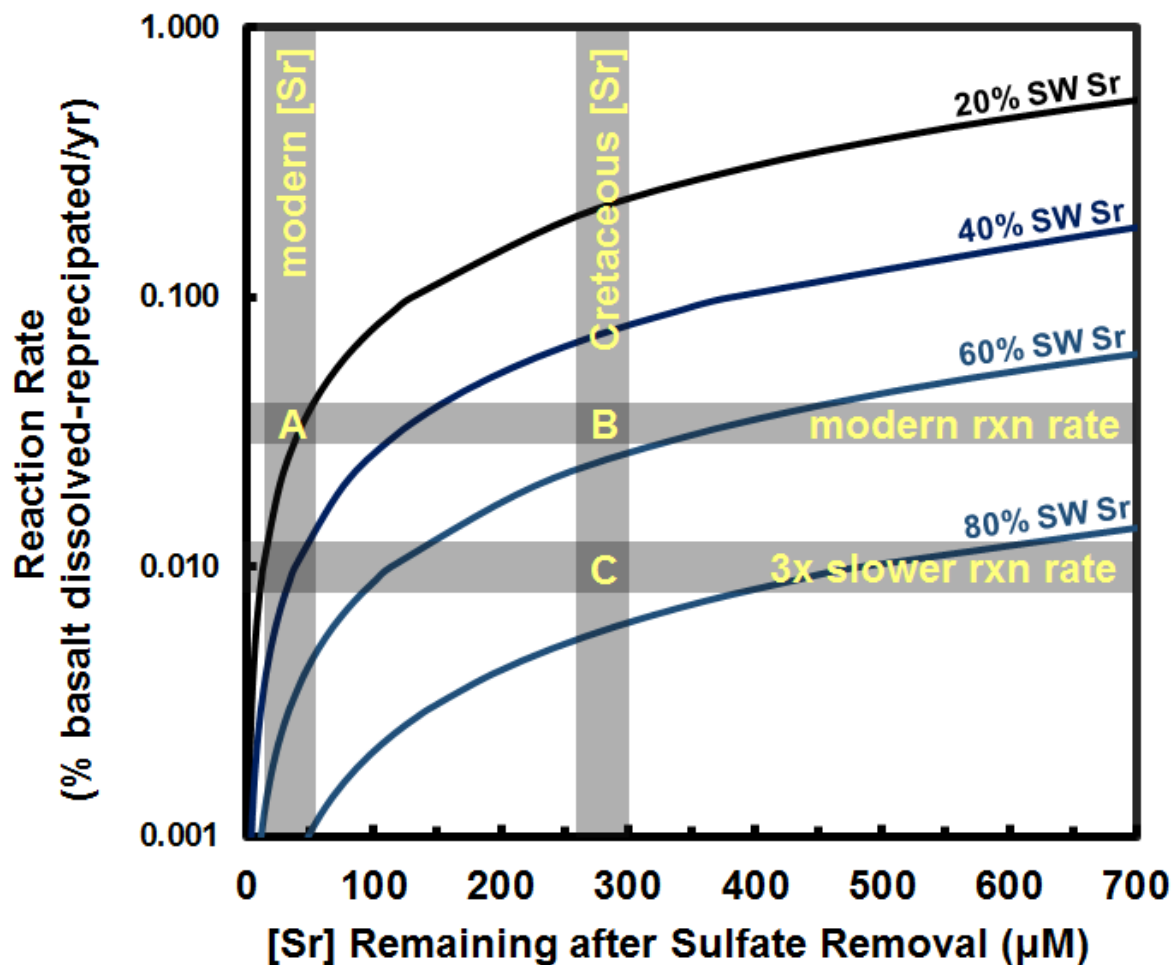


Fig. S5. Hydrothermal output $^{87}\text{Sr}/^{86}\text{Sr}$ compositions (as % seawater Sr, plotted as curves) as functions of reaction rate and seawater [Sr] remaining after full removal of seawater sulfate as anhydrite, calculated using a steady-state dual porosity model (17) described in the SI text. Vertical and horizontal bars demarcate modern [Sr], modern reaction rate (0.03 yr^{-1}), estimated Cretaceous [Sr], and an arbitrarily 3x slower reaction rate (0.01 yr^{-1}). At “A” exiting fluid has ~18% seawater Sr. At “B” exiting fluid has ~55% seawater Sr, and at “C” exiting fluid has 71% seawater Sr; these represent hydrothermal fluid $^{87}\text{Sr}/^{86}\text{Sr}$ of 0.7037, 0.7062, and 0.7073, respectively. Other parameters: fracture fluid velocity = 820 m/yr, fracture width = 5 cm, fracture spacing = 2 m, matrix porosity = 0.01.